PUBLICATIONS OF THE ASTRONOMICAL SOCIETY OF THE PACIFIC, **120**:328–338, 2008 March

Absolute Calibration and Characterization of the Multiband Imaging Photometer for *Spitzer*. IV. The Spectral Energy Distribution Mode

NANYAO LU, [1] PAUL S. SMITH, [2] CHARLES W. ENGELBRACHT, [2] ALBERTO NORIEGA-CRESPO, [1] JANE MORRISON, [2] KARL D. GORDON, [2], JOHN STANSBERRY, [2] FRANCINE R. MARLEAU, [1] GEORGE H. RIEKE, [2] ROBERTA PALADINI, [1] DEBORAH L. PADGETT, [1] JOCELYN KEENE, [1] WILLIAM B. LATTER, [1] DARIO FADDA, [1] AND JEONGHEE RHO[1]

Received 2007 November 14; accepted 2008 January 22; published 2008 March 13

ABSTRACT. The spectral energy distribution (SED) mode of the Multiband Imaging Photometer for *Spitzer* (MIPS) aboard the *Spitzer Space Telescope* provides low-spectral resolution (R $\approx$ 15–25) spectroscopy in the far-infrared using the MIPS 70 μm detector. A reflective grating provides a dispersion of 1.7 μm per pixel, and an effective wavelength coverage of 52.8–98.7 μm over detector rows 1–27. The final 5 detector rows are contaminated by second-order diffracted light and are left uncalibrated. The flux calibration is based on observations of MIPS calibration stars with 70 μm flux densities of 0.5–15 Jy. The point-source flux calibration accuracy is estimated to be 10% or better down to about 0.5 Jy at the blue end of the spectrum and to ~2 Jy near the red end. With additional uncertainties from the illumination and aperture corrections included, the surface brightness calibration of extended sources is accurate to ~15%. Repeatability of better than 5% is found for the SED mode through multiple measurements of several calibration stars.

1. INTRODUCTION

The spectral energy distribution (SED) mode of the Multiband Imaging Photometer for *Spitzer* (MIPS; Rieke et al. 2004) aboard the *Spitzer Space Telescope* (hereafter *Spitzer*; Werner et al. 2004) provides a capability for obtaining long-slit, low-resolution (R $\approx$ 15–25) spectra in the far-infrared (53–98 μm). This extends *Spitzer*'s spectroscopic wavelength coverage to beyond that of the higher-resolution Infrared Spectrograph (Houck et al. 2004) that operates up to 40 μm. The SED slit is two detector pixels (~20″) in width, and 12 pixels (~2′) in length where the full wavelength coverage is available. An inoperative detector module restricts the wavelength coverage to only 67–98 μm over the last 4 columns of the detector array of 16 columns times 32 rows.

Observations with *IRAS* and the *Infrared Space Observatory* (*ISO*) have shown that most starburst galaxies and active galactic nuclei have their far-infrared dust emission peaking between 50 and 100 μm. The MIPS SED mode is well tailored to capture a spectral section around the peak of the dust emission, and thus can provide a good constraint on the temperatures and masses of the bulk of dust particles in these energetic systems. Although it has a lower spectral resolution than the *ISO* long-wavelength spectrometer (LWS), the MIPS SED mode is more sensitive (e.g., at 60 μm, the 5 σ continuum sensitivity of 82 mJy in a 500-sec on-target integration achieved in the MIPS SED mode for point sources is roughly 3 times that of the *ISO* LWS integrated over the wavelength coverage of each MIPS SED pixel; see Gry et al. 2003). It also provides more spatial information and has demonstrated an improved degree of repeatability. The MIPS SED mode has been used by *Spitzer* observers for various projects, ranging from determining galaxy spectral energy distributions in the far-infrared (e.g., Kennicutt et al. 2003) to characterizing circumstellar dust emission (e.g., Low et al. 2005).

Using the same detector and internal stimulators (STIM), the SED mode shares many calibration characteristics (e.g., dark current) with the 70 μm imaging photometry mode. The calibration of the latter is described in detail by Gordon et al. (2007; hereafter GEF07). In this paper, we first give a brief overview of the operation and calibration principles of the MIPS SED mode (§ 2) and then describe in more detail specific calibration issues, including illumination correction (§ 3), wavelength calibration (§ 4), aperture corrections (§ 5), and flux calibration (§ 6). A summary is given in § 7.

2. OPERATION AND CALIBRATION PRINCIPLES OF THE MIPS SED MODE

The astronomical observing template of the SED mode, as illustrated in Figure 1, provides pairs of data frames between the target position (ON) and a nearby sky position (OFF). The MIPS scan mirror is used to chop between ON and OFF, and an observer can choose chop throws of $+3'$, $+2'$, $+1'$, or $-1'$ on the sky. The observer can request either a pointed observation or an $M \times N$ raster map of a larger region (with M, N between 1 and 100). For a pointed observation (or at each

[1] *Spitzer Space Telescope* Science Center, MS 314-6, California Institute of Technology, Pasadena, CA; lu@ipac.caltech.edu

[2] Steward Observatory, The University of Arizona, Tucson, AZ

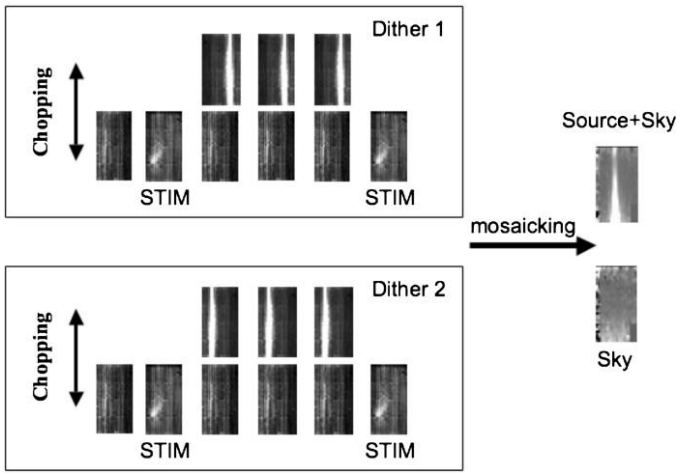

FIG. 1.—Sketch of the basic set of frames taken with the astronomical observing template of the MIPS/SED mode. The sequence of the observation is from left to right. Dithers are carried out by simple spacecraft offset, while the chopping is carried out by the cryogenic scan mirror mechanism. For both dither positions, STIM frames are always taken at the background position. Final images of the target plus background and background alone are produced by combining appropriate individual frames in mosaic.

raster position in the case of a map), there is a basic set of 6 pairs of ON and OFF frames. The first 3 pairs of data-collection events (DCEs), each of ~10 s (or 3 s if observing very bright sources) in duration, are obtained with the target placed near the center of detector column 10 (hereafter referred to as dither position 1) and the next 3 pairs with the target near the center of column 5 (dither position 2). The telescope is moved to position the target on the dither positions. Bracketing each of the 3 pairs of DCEs are STIM exposures to track detector responsivity variations. Each STIM is preceded by a DCE at OFF. The observer repeats this basic set by specifying a number of cycles (N_c) in order to reach the desired signal-to-noise ratio (S/N). For a mapping observation, the value of N_c remains the same for all the raster positions.

The basic instrumental calibration of the SED mode is similar to that of the 70 μm imaging mode and follows equations (4) to (16) in Gordon et al. (2005; hereafter GRE05). The single difference is that in the SED mode, the detector Y-axis coincides with the spectral dispersion axis. As a result, an illumination correction (IC) frame obtained from some sky position in the SED mode contains a wavelength-dependent factor, Z, inherited from the intrinsic spectral signature of the sky emission (cf. § 3). Equation (15) of GRE05 can be modified for the SED mode as follows:

$$U_{\rm illum}(i,j) = Z(j)O(i,j)/S(i,j), \tag{1}$$

where i and j are respectively the detector column and row indices, $O(i,j)$ is the combined optical response of the telescope and instrument, and $S(i,j)$ is the STIM illumination pattern. Since j correlates linearly with wavelength (cf. § 4), we have expressed Z as a function of j in equation (1).

The responsivity-corrected, dark-subtracted, and IC-corrected data frame of equation (16) in GRE05 becomes

$$U_{\rm data}(i,j) = I(i,j)/Z(j), \tag{2}$$

where $I(i,j)$ is the spectral image of the sky projected onto the detector array.

The subsequent flux calibration of equation (2) converts MIPS (instrumental) units to Jy. This is accomplished via observations of standard stars (cf. § 6), from which we derive a mean nominal spectral response function, R, for the SED mode:

$$R^{-1}(j) = f_\nu(j)C^{-1}_{\rm aper}(j)/\left[\sum_{i=1}^{N} I_{\rm sub}(i,j)/Z(j)\right], \tag{3}$$

where the summation represents the spectral extraction within a predefined aperture of N columns times 1 row, $f_\nu(j)$ is the known stellar flux density at the central wavelength of detector row j, $C^{-1}_{\rm aper}(j)$ is the corresponding aperture-correction factor so that $f_\nu(j)C^{-1}_{\rm aper}(j)$ is the net flux density within the chosen aperture, and $I_{\rm sub}(i,j)$ is the sky-subtracted signal from the target star. The nominal spectral response differs slightly from the conventionally defined spectral response function, R_0, commonly seen in the literature: $R(j)Z(j) = R_0(j)$. Since $Z(j)$ appears in both equations (2)and (3), it is removed from the data during flux calibration.

Calibration observations of the SED mode were reduced using the MIPS Data Analysis Tool (DAT, v2.96, see GRE05). The results presented here are derived from either the co-added images at a given dither position or a mosaic image from both dither positions. The image pixel scale is always kept equal to the detector pixel size of $9.8'' \times 9.8''$.

3. ILLUMINATION CORRECTION

3.1. Observational Results

The characterization of the combined effects of a nonuniform illumination pattern and the difference in illumination between sky and the undispersed STIM flashes can be calibrated by imaging celestial sources of uniform surface brightness (GRE05). The Zodiacal light is generally too faint for deriving such an IC for the SED mode. Instead, we have utilized SED observations of diffuse Galactic emission (with *IRAS* $I_\nu(60\ \mu m)/I_\nu(100\ \mu m) \sim 0.2$–$0.3$) near the Galactic plane. Once an adequate number of independent observations have been acquired, median filtering is performed to exclude any spatial structure that might be present in individual fields. To reach an adequate signal level (i.e., ~5–10 times the level of the dark current), we targeted regions where *IRAS* $I_\nu(60\ \mu{\rm m}) = 200$–$300$ MJy sr^{-1} and where no *IRAS* point sources are identified within a radius

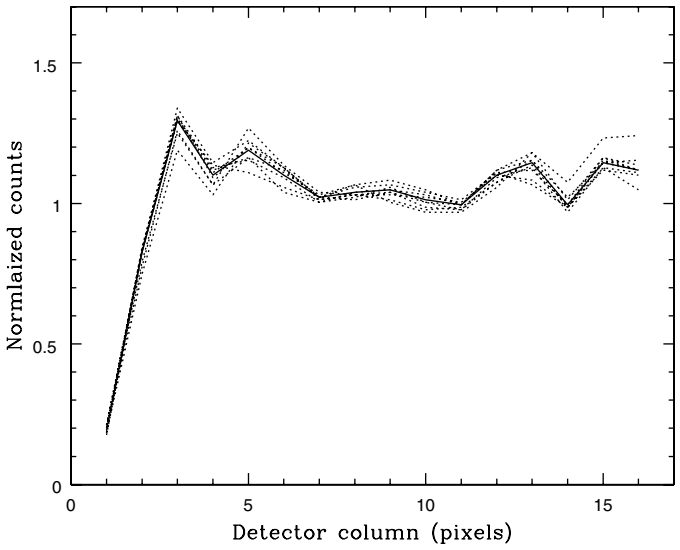

FIG. 2.—Plot of the average spatial profile (*dotted lines*) over detector rows 9–15 for each of the 9 IC observations acquired between MIPS campaigns 20 and 24. The thick solid curve shows the median result.

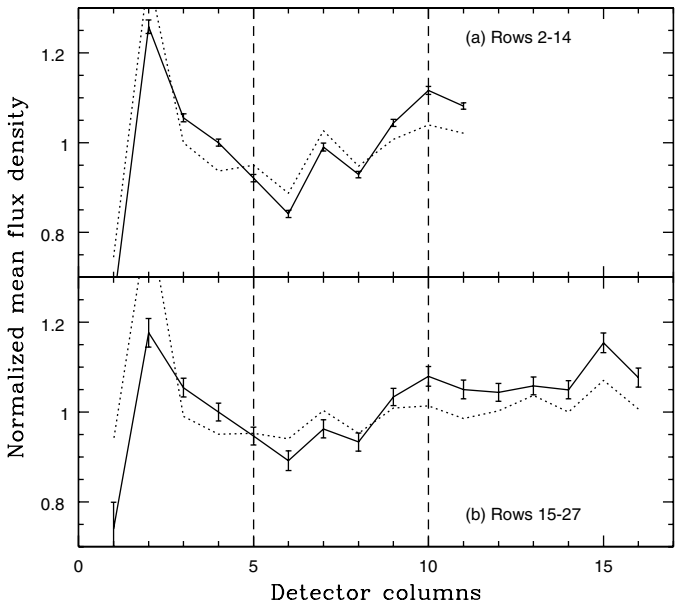

FIG. 3.—Plots of the observed average signal (*solid lines*) from Arp 231 using a three-column aperture at each of the 16 *Spitzer* positions of a raster-map observation. Panel (*a*) is averaged over detector rows 2–14 (55–75 μm) and (*b*) over rows 15–27 (77–97 μm). A column correction (see § 3.2 and Table 1) yields the dotted curves. The two dashed vertical lines indicate the default dither positions. The truncation of the data in panel (*a*) beyond column 11 is due to the inoperative detector module. Note that the first two flux points in each plot are affected by the first detector column, which is much noisier than the other columns. Excluding these first two data points, the dotted curve in each plot shows a variation of $\sim$5%.

of $\sim 5'$–$10'$. Each of the selected regions is observed in a 4×1 map with a chop throw of $2'$.

Individual observations were examined for signs of "bad" sky positions (e.g., a point source accidentally in the slit), and a subset was chosen for median filtering to generate a final IC image. As an illustration, Figure 2 compares the individual IC observations by plotting their normalized mean spatial profiles, together with the resulting median.

Figure 2 reveals that the instrumental sensitivity drops substantially for the first couple of detector columns. A possible explanation could be that the end of the slit vignettes these detector columns. The first detector column also shows a much greater pixel-to-pixel noise level compared with the other detector columns. This entire column is masked out in the S17 and later versions of the MIPS SED-mode data-reduction pipeline.

3.2. Residual Systematics

The adopted approach to constructing the IC is quite efficient, reaching high signal levels over the entire detector array in a reasonable amount of telescope time. However, there are some residual systematic variations of up to $\sim 15\%$ along the spatial axis of the slit. This effect is illustrated in Figure 3 using the data from a 16×1 mapping observation of the point-source–like galaxy Arp 231. The target was scanned along the slit with a step size that matches the detector pixel size. For each raster pointing, the ON frames from one of the two default dither positions have been co-added and sky-subtracted, and a three-column aperture was used to extract a spectrum. The results from the map are shown in Figure 3 for two detector row ranges.

Figure 3 reveals two important characteristics: (1) Excluding the noisy first detector column (which affects the first two data points in each plot), there is a flux variation of up to 10%–15% from column to column. (2) This column-to-column variation has only a weak dependence on wavelength. Since the amplitude of this residual systematic variation appears to scale with incident flux, a first-order empirical correction can be made by averaging a number of observations similar to that of Arp 231. Table 1 lists a simple column correction derived from two such mapping observations. Dividing the values in Table 1 into the IC image by column leads to a composite IC that reduces the

TABLE 1
COLUMN DIVISION FACTORS TO IC

Det. Col.	Correction	Det. Col.	Correction
1	0.529	9	1.008
2	1.102	10	1.082
3	0.995	11	1.026
4	1.099	12	1.052
5	0.938	13	0.958
6	0.919	14	1.045
7	0.956	15	1.098
8	0.948	16	1.005

residual flux variation to ~5% (except for the first detector column) and brings the flux measured between the two default dither positions into reasonable agreement for the observed calibration stars. This composite IC is used throughout this paper.

4. WAVELENGTH CALIBRATION

The formal dispersion solution was based on two observations of the bright planetary nebula NGC6543 that shows prominent [N III] 57.330 μm and [O III] 88.356 μm emission lines. The two observations are identified by Astronomical Observation Request (AOR) tags of 13437952 and 20719616, respectively.

Each observation of NGC 6543 was reduced independently. The sky-subtracted, mosaic images from the two observations were averaged together; a spectrum was subsequently extracted using a five-column aperture and is shown in Figure 4. The MIPS instrument design yields, to first order, a linear dispersion, and the instrumental optical model suggests that the bandpass of each detector pixel only varies by $\pm 1.5\%$ from the nominal value. Assuming uniform dispersion, the measured line positions yield a dispersion of 1.70 μm per pixel and a wavelength of 53.66 μm for the center of the first detector row at the blue end of the spectrum.

Each line fitting uses four independent data points; the wavelength calibration uncertainty is thus estimated to be on the order of 0.4 μm ($\approx 0.5 * 1.7\ \mu\mathrm{m}/\sqrt{4}$) for uniform dispersion. Differences in line positions among various line profile fitting methods (e.g., centroiding using moments) are all within this uncertainty estimate. For a given centroiding method, the differences in the emission-line positions between the two observations of NGC 6543, obtained about 19 months apart, are on the order of 0.1 μm.

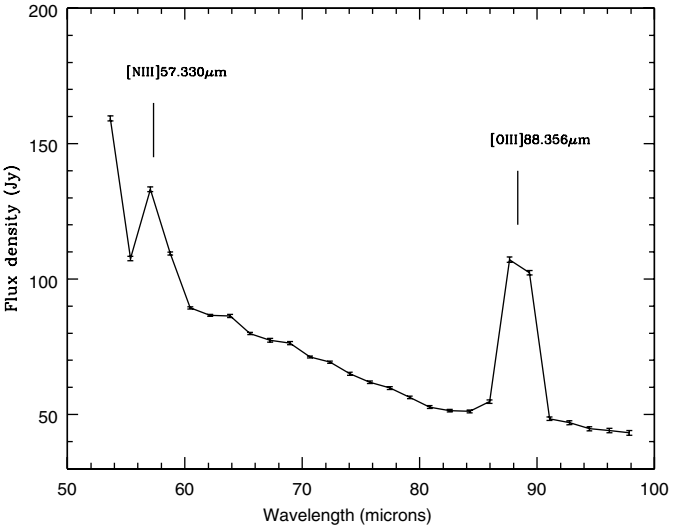

FIG. 4.—Average SED-mode spectrum of the planetary nebula NGC 6543 derived from observations made in MIPS Campaigns 20 and 36. The spectrum is extracted with a five-column (~50″) aperture.

TABLE 2
APERTURE CORRECTIONS

Det. Row (1)	$\lambda(\mu$m) (2)	C(2cols) (3)	C(3cols) (4)	C(4cols) (5)	C(5cols) (6)
1	53.66	1.931	1.763	1.673	1.591
2	55.36	1.961	1.785	1.701	1.616
3	57.06	1.991	1.807	1.729	1.642
4	58.76	2.022	1.829	1.757	1.668
5	60.46	2.055	1.851	1.785	1.695
6	62.16	2.095	1.874	1.809	1.724
7	63.86	2.134	1.896	1.833	1.752
8	65.56	2.174	1.918	1.857	1.781
9	67.26	2.214	1.941	1.881	1.810
10	68.96	2.254	1.963	1.905	1.838
11	70.66	2.297	1.988	1.929	1.867
12	72.36	2.347	2.016	1.951	1.894
13	74.06	2.397	2.044	1.974	1.921
14	75.76	2.447	2.072	1.997	1.948
15	77.46	2.497	2.100	2.019	1.975
16	79.16	2.547	2.128	2.042	2.003
17	80.86	2.602	2.160	2.065	2.029
18	82.56	2.662	2.194	2.090	2.054
19	84.26	2.721	2.229	2.114	2.079
20	85.96	2.781	2.264	2.139	2.104
21	87.66	2.840	2.298	2.163	2.129
22	89.36	2.900	2.333	2.188	2.154
23	91.06	2.965	2.372	2.215	2.179
24	92.76	3.033	2.414	2.243	2.204
25	94.46	3.102	2.455	2.272	2.229
26	96.16	3.170	2.497	2.300	2.254
27	97.86	3.239	2.539	2.329	2.279

NOTE.—Derived from the *Spitzer* Tiny Tim model smoothed by a square box of a width equal to the detector pixel size.

The effective wavelength coverage over detector rows 1–27 of the SED mode is 52.8–98.7 μm and the wavelength assignments for each detector row are listed in column (2) of Table 2. The remaining 5 detector rows at wavelengths > 98 μm are contaminated by shorter wavelength, second-order light and are left uncalibrated.

5. APERTURE CORRECTIONS

In Figure 5, the observed mean spatial profiles at 70 and 90 μm are shown in comparison with the predicted point spread functions (PSF) from the *Spitzer* Tiny Tim model (Krist 2002). The measured profiles were derived from the average of nine observations of three bright stars through MIPS Campaign (MC) 24 in 2005 August. Averaging was independently done at each dither position to test if the PSF has a dependence on array position. We averaged detector rows 10 and 11 to produce the spatial profile at 70 μm. Detector rows 22 and 23 were averaged for an estimate of the PSF at 90 μm. The abscissa of Figure 5 is the distance along the slit length, measured from the corresponding profile peak. Because of a small spectral tilt, the

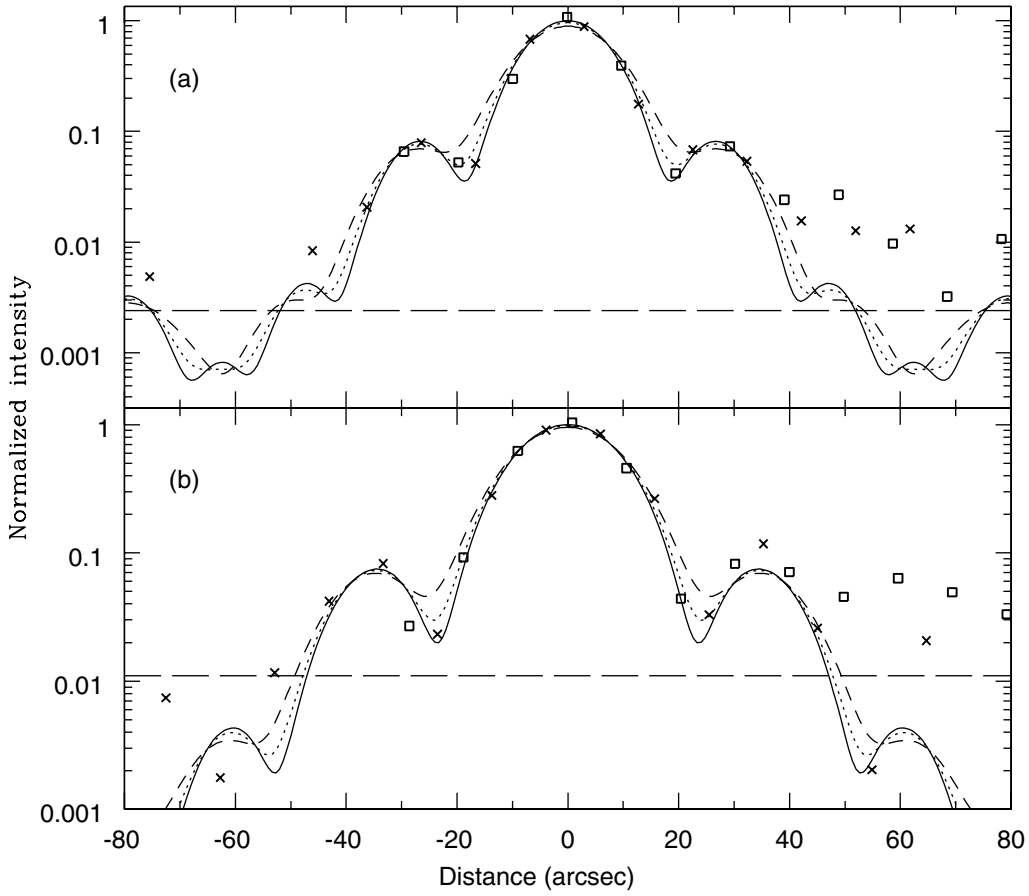

FIG. 5.—Comparisons of the observed mean spatial profiles (*points*) with the model predictions (*curves*) at 70 μm (*a*) and 90 μm (*b*). The measured profiles are shown separately for dither positions 1 (*crosses*) and 2 (*squares*) and are derived from the observations of the bright calibration stars. The model curves are those of the *Spitzer* Tiny Tim model smoothed by a boxcar of width of D = 1.0 (*solid curves*), 1.3 (*dotted curves*), or 1.7 (*dashed curves*) times the detector pixel size of 9.8″.

profile center location on the detector array has a small dependence on wavelength. We smoothed the fine-sampled Tiny Tim model image with a square box of width D = 1, 1.3, and 1.7 times the detector pixel size, and derived a predicted PSF by integrating the smoothed image over the slit width of 2 pixels. All of the model profiles were normalized so that they yield the same intensity sum from the three sampled positions closest to the profile peak at dither position 1; the measured profile from dither position 2 was then normalized in a similar way with respect to the model profile of D = 1.

The measured PSF for the SED mode matches the Tiny Tim models very well at small radii. For radii that encompass the first Airy ring, the measurements agree best with the D = 1 model curve, although the sparse sampling does not allow for the D = 1.3 model to be robustly ruled out. At large positive distances (45″–60″), the observed profile appears to be broader than the model predictions. However, the excess has a significance of only 2–2.5 σ. Better agreement with the model predictions is seen at large negative distances. The magnitude of the observed excess, its asymmetry, and the fact that it is seen at

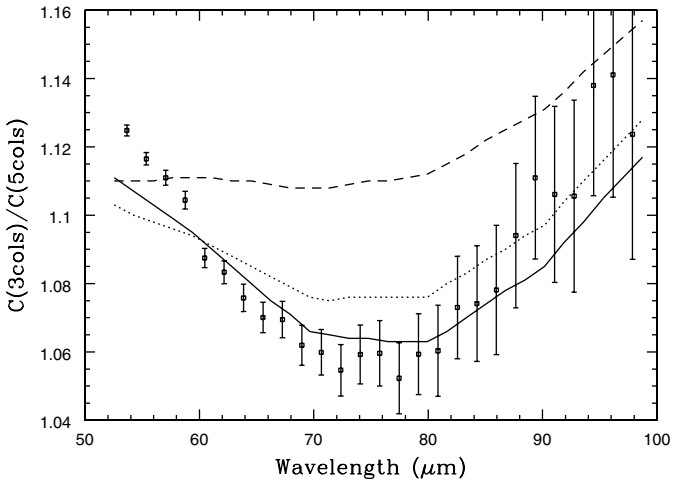

FIG. 6.—Comparison between the observed (*squares*) and Tiny Tim model predictions (*curves*) of the three-column to five-column aperture-correction ratio, C(3cols)/C(5cols). The three model results shown here are denoted in the same manner as in Fig. 5.

TABLE 3
OBSERVATIONS OF SED CALIBRATION STARS

Star (1)	Type (2)	f_{mod}(unc.)[a] (Jy) (3)	f_{MIPS}[b] (Jy) (4)	f_{SED}[c] (Jy) (5)	$(S/N)_{SED}$[d] (6)	N_c (7)	MC (8)	AOR (9)
HD 006860	M0III	5.33(0.20)	5.36	5.47	49	9	24	15811840
HD 018884	M1.5III	4.64(0.16)	4.61	4.96	28	6	18	13124352
HD 029139	K5III	12.84(0.45)	11.41	13.13	73	6	19	13309440
HD 045348	F0II	3.08(0.07)	2.94	2.96	22	9	18	13124608
				2.95	22	9	19	13309952
				2.98	22	9	21	13615872
HD 051799	M1III	0.59(0.02)	0.61	0.70	7	12	19	13310208
HD 060522	M0III	0.75(0.02)	0.73	0.80	8	12	20	13440256
HD 062509	K0IIIb	2.61(0.08)	2.62	2.65	25	9	20	13440000
HD 070272	K4.5III	0.55(0.02)	…	0.59	6	12	20	13440512
HD 081797	K3II-III	2.89(0.10)	2.97	2.88	23	9	21	13616384
HD 082308	K5III	0.54(0.02)	0.51	0.49	5	12	21	13616640
HD 082668	K5III	1.42(0.20)	1.49	1.30	6	6	7	9655552
HD 091056	M0III	0.45(0.10)	…	0.78	6	12	18	13124864
				0.52	4	12	19	13310464
				0.63	6	18	23	15423488
HD 108903	M3.5III	17.00(1.77)	16.16	19.08	91	6	18	13123840
				18.77	89	6	19	13309184
				19.00	90	6	22	15248640
				18.98	90	6	23	15422720
HD 120477	K5.5III	0.67(0.02)	…	0.78	7	12	18	13125120
				0.68	7	15	22	15249408
HD 123123	K2III	0.49(0.02)	0.44	0.48	6	18	23	15423744
HD 124897	K1.5III	14.34(0.78)	13.60	14.32	69	6	10	11625216
				14.67	70	6	18	13124096
				14.55	70	6	22	15248896
				14.63	70	6	23	15422976
HD 131873	K4III	3.36(0.12)	3.31	3.32	28	9	21	13616128
HD 137759	K2III	0.50(0.02)	…	0.63	6	15	22	15249664
HD 150798	K2II-III	2.99(0.09)	…	2.92	23	9	20	13439744
HD 164058	K5III	3.31(0.10)	3.38	3.32	25	9	19	13309696
				3.22	24	9	20	13439232
				3.25	24	9	21	13615616
				3.19	24	9	22	15249152
				3.17	24	9	23	15423232
HD 198542	M0III	0.82(0.04)	0.81	0.86	8	12	21	13616896
HD 211416	K3III	1.27(0.05)	…	1.30	6	6	7	9657856

[a] Model-predicted flux density at 71.42 μm from Engelbracht et al. (2007) with the uncertainty given in parentheses.
[b] MIPS photometric flux density at 71.42 μm from GEF07.
[c] SED-mode measured flux density at 71.42 μm (see the text).
[d] S/N ratio of the SED-mode measurement.

both dither positions make it unlikely that this effect is caused by either IC residual systematics or detector flux nonlinearity.

In columns (3)–(6) of Table 2, we have calculated the aperture-correction factors (C) using the $D = 1.0$ model for extraction aperture sizes of two to five detector columns *centered* on an unresolved target. The difference in aperture corrections between $D = 1.0$ and $D = 1.3$ is less than 2% at any wavelength. The aperture-correction ratio between the three- and five-column aperture sizes in Table 2 can also be measured using the bright calibration stars and the result is compared in Figure 6 with various model predictions. It is evident that the data agree best with the $D = 1$ case, and are within 2%–3% of the model predictions.

About 10% of the flux lies outside the radius of 50″ in the case of $D = 1$. In contrast, the measured PSF is roughly twice as bright as the $D = 1$ model prediction at radii $\gtrsim$50″. This implies

that the flux calibration for an extended source using the aperture-correction factors in Table 2 could be off by up to 10% if this "light excess" at large radii originates from the PSF core and affects a large fraction of the PSF disk.

6. FLUX CALIBRATION

6.1. Calibration Stars

The primary flux calibrators for the SED mode are moderate to bright stars from a list compiled for the flux calibration of the MIPS 70 μm photometric mode (GEF07). Their effective photospheric temperatures, T_e, and model flux densities at 71.42 μm, $f_\nu(71.42)$, are given in Engelbracht et al. (2007), where 71.42 μm is the effective wavelength of MIPS broadband 70 μm photometric system. The model spectrum of a star over the spectral range of the SED mode is simply represented as a Planck function with $T = T_e$ anchored at an adopted $f_\nu(71.42)$, which can be either the model prediction from Engelbracht et al. (2007) or the MIPS 70 μm photometric observation from GEF07. Note that for stars, the color correction necessary to convert a MIPS 70 μm photometric measurement to a monochromatic flux density is unity.

Because the effective sensitivity of the SED mode on stars decreases steeply as wavelength increases, we have chosen calibration stars in three flux ranges of $f_\nu(71.42)$: (1) three stars brighter than 10 Jy, (2) eight moderately bright stars with $f_\nu(71.42) = 2$–6 Jy, and (3) 11 "faint" stars with $0.45\ \mathrm{Jy} < f_\nu(71.42) < 2$ Jy. Observations were made (except during a couple of early MIPS campaigns) so that $\mathrm{S/N} \gtrsim 10$ was reached for stars in range (1) over the entire spectrum, for stars in range (2) shortward of ~80 μm, and for those in range (3) shortward of 65–70 μm. This tiered strategy allows for reasonable integration times at all three flux levels, and it tests whether there is a significant flux nonlinearity in the detector responsivity.

Table 3 lists observations of the calibration stars through 2005 August (i.e., MC24). The table columns are (1) the star catalog name, (2) the spectral type, (3) the model $f_\nu(71.42)$ from Engelbracht et al. (2007) with the flux uncertainty given in the parentheses, (4) the MIPS-measured $f_\nu(71.42)$ by GEF07 using their PSF fitting method, (5) a $f_\nu(71.42)$ derived from the SED-mode measurement using the aperture-correction factors in Table 2 and the spectral response function in Table 4, of which the derivation is explained in § 6.2, (6) the S/N ratio of the SED-mode measurement, (7) the number of cycles executed in the SED observation, (8) the MIPS campaign number, and (9) the AOR tag in the *Spitzer* data archive. The uncertainty for the flux densities in column (4) is taken to be 5% (see GEF07).

A number of the calibration stars in Table 3 have been observed in multiple campaigns. These include stars in all three flux level categories. The SED-mode results for these stars (when measurement S/N ratios are high enough, e.g., $\mathrm{S/N} > 15$) indicate a stable instrument performance with time. Repeatability of ~2% and $\lesssim$5% were measured at the blue and red ends of the spectrum, respectively.

TABLE 4

MEAN INVERSE NOMINAL SPECTRAL RESPONSE FUNCTION

Row (1)	λ (μm) (2)	$(R^{-1})^a$ (MJy sr^{-1}/MIPS) (3)	$\sigma_{\mathrm{mean}}{}^b$ (4)	Stars (5)
1	53.66	7695	108	19
2	55.36	8440	126	19
3	57.06	9695	128	19
4	58.76	10576	153	19
5	60.46	11453	142	19
6	62.16	12775	159	19
7	63.86	14194	195	17
8	65.56	14792	216	15
9	67.26	16524	314	13
10	68.96	17293	221	12
11	70.66	19031	227	10
12	72.36	20141	230	10
13	74.06	21327	288	10
14	75.76	22620	329	10
15	77.46	23606	352	10
16	79.16	24616	228	10
17	80.86	27105	423	10
18	82.56	27845	402	10
19	84.26	29469	618	7
20	85.96	31197	429	6
21	87.66	33085	683	5
22	89.36	34751	771	5
23	91.06	35385	750	5
24	92.76	35992	497	5
25	94.46	38665	821	4
26	96.16	38647	1671	3
27	97.86	39349	1010	3

[a] R^{-1} is as defined in eq. (3) in the text with the aperture-correction factor from Table 2.

[b] Sample standard deviation of the mean as given in eq. (4) in the text.

6.2. Nominal Spectral Response Function

For each observation of a calibration star, the spectrum was extracted from the sky-subtracted mosaic image using a five-column aperture. If a star was observed multiple times, the resulting spectra were averaged.

Figure 7 compares 71.42 μm flux density ratios between (i) the SED mode, (ii) the photospheric model predictions, and (iii) MIPS 70 μm PSF-fitted photometry for the calibration stars. For the purpose of these figures, the SED-mode flux scale was simply derived by using a flux conversion factor that results in the median flux density ratio of (ii) to (i) $\approx$1 for stars with $f_\nu(71.42) > 1$ Jy. While there is no apparent flux dependency in the ratio between the model predictions and the SED-mode results, the three brightest stars are significantly below 1 in both Figure 7*a* and *b*. These stars are at the high end of the flux range calibrated for the MIPS photometric system (GEF07), and,

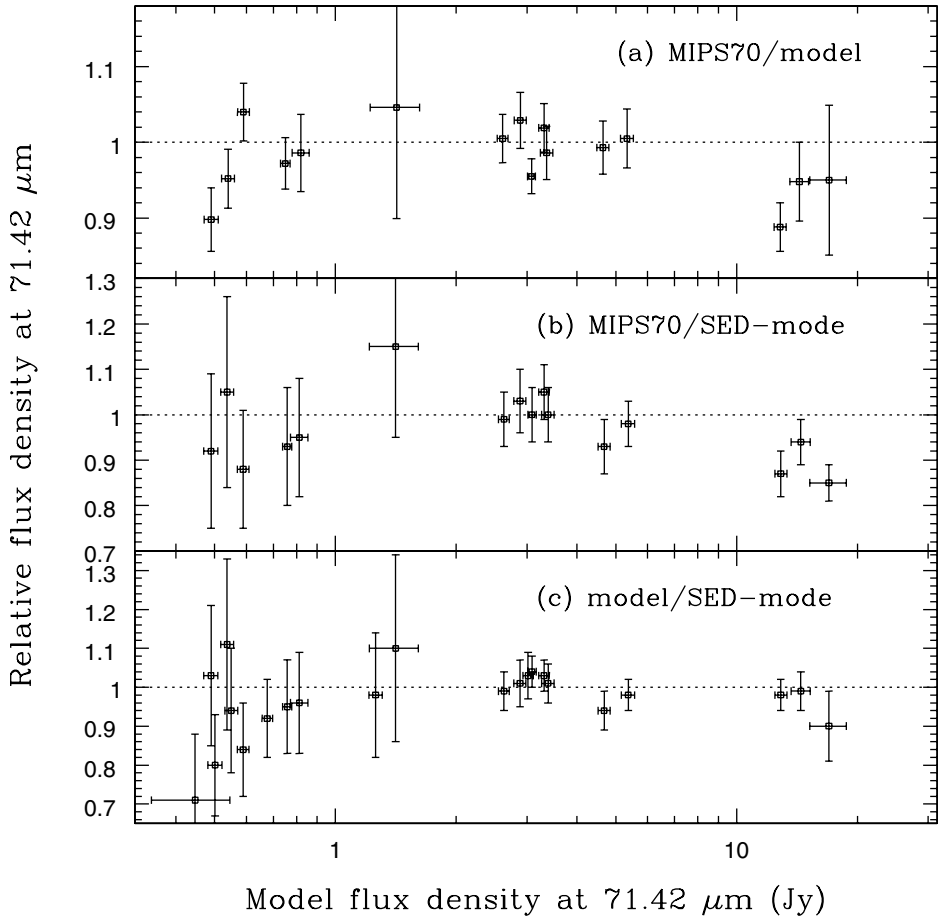

FIG. 7.—Various 71.42 μm flux density ratios as a function of the model-predicted flux density at 71.42 μm. Panels (*a*) and (*b*) display the MIPS 70 μm photometric measurement relative to the model prediction and the SED-mode measurement, respectively. Panel (*c*) shows the ratio of the model prediction to the SED-mode measurement. The (relative) SED-mode flux densities were derived using a conversion factor that yields a sample median for (*c*) close to 1 for those stars with $f_\nu(71.42) > 1$ Jy.

therefore, their 70 μm photometric fluxes may suffer some moderate flux nonlinearity. These stars are crucial in the SED-mode flux calibration because they are the only measurements having high S/N at the red end of the spectrum, and so we chose to base the SED-mode flux calibration on the photospheric model predictions. The model predictions are consistent with the MIPS 70 μm photometric fluxes below ~10 Jy.

The SED-mode spectrum of each calibration star was aperture-corrected and divided into the adopted stellar model spectrum to yield the inverse of the nominal spectral response function, R^{-1}, in units of Jy per MIPS unit, where R is as defined in equation (3). We used an inverse noise-squared weighting to determine the average R^{-1}. In addition, at a given wavelength, a star is rejected if the S/N < 10.

Table 4 gives the resulting mean nominal spectral response function in the standard *Spitzer* units of MJy sr^{-1} per MIPS unit, where $1\ \mathrm{Jy} = 443\ \mathrm{MJy\ sr^{-1}} \times (9.8'' \times 9.8'')$. The results in Table 4 also reflect the MIPS data reduction pipeline convention that has the IC normalized by its median within the image section [2:16,1:31]. The quoted uncertainty in R^{-1} is the sample standard deviation of the mean, σ_{mean}, given by

$$\sigma^2_{\mathrm{mean}} = \frac{1}{(\Sigma w_i)^2/\Sigma w_i^2 - 1}\left(\frac{\Sigma w_i r_i^2}{\Sigma w_i} - \langle r\rangle^2\right), \qquad (4)$$

where r_i and w_i are respectively the response and weight from the ith sample star, and $\langle r\rangle$ is the weighted mean response. Finally, the actual number of stars averaged at each wavelength is given in column (5).

As discussed in § 2, the nominal spectral response function includes the spectral signature of the diffuse Galactic emission via the IC used in the data reduction. Thus, R^{-1} *changes* if a *different* IC is used in the data reduction.

6.3. Absolute Flux Accuracy and Cross Comparisons

Flux or wavelength-dependent systematic errors in the SED-mode flux calibration can be checked by comparison with model predictions for the calibration stars at various represen-

tative wavelengths. Such a comparison at 71.42 μm is displayed in Figure 7*c*. In Figure 8, similar plots are shown for $\lambda \approx 60$, 75, and 90 μm. In these plots, the Planck function model spectrum for each star is normalized to the MIPS 70 μm photometric flux density. As expected, the SED-mode flux densities have fairly large uncertainties at both 75 and 90 μm for stars with $f_\nu(71.42) < 2$ Jy. In spite of this, the flux density ratios do not appear to have any obvious dependency on flux at the three selected wavelengths outside of the three brightest stars that may have their MIPS 70 μm photometric flux densities underestimated by 5%–10%. A check of the uncertainty in the determination of the flux calibration is offered by the scatter in the data points plotted in Figure 8. The scatter is $<10\%$ at 60 μm down to at least 0.5 Jy and down to ~2 Jy at 90 μm.

Comparisons with the results from past spacecraft suggest that the absolute flux calibration of the SED mode is accurate to 10% or better for point sources. For example, Figure 9 compares the MIPS SED-mode spectra of the galaxies NGC 4418 and Mrk 231 with *IRAS* measurements at 60 and 100 μm. Also shown in Figure 9 is an *ISO* LWS spectrum of Mrk 231. Generally, the data agree to within 10%. These comparisons also suggest that flux nonlinearity for the SED mode is insignificant over a 70 μm flux density range of 0.5–40 Jy.

6.4. Extended-Source Flux Calibration

Since the SED-mode flux calibration is based on stars, uncertainties in the aperture correction and the IC systematic effect described in § 3.2 have little impact on the calibration of a point source. However, these do introduce additional uncertainty in the surface brightness calibration of an extended source. Although difficult to quantify because of the lack of available SED-mode observations of well-calibrated extended sources, Table 5 summarizes an estimated error budget for this case. The total uncertainty in flux density is estimated to be on the order of 15% or less.

The galaxy merger system Arp299 offers an opportunity to evaluate the performance of the MIPS SED mode for an extended source. It was observed using a 4×1 raster map (AOR = 12919296) centered at R.A. = $11^h28^m32.3^s$ and decl. = $58°33'43''$ (J2000.0) and with the slit oriented at a

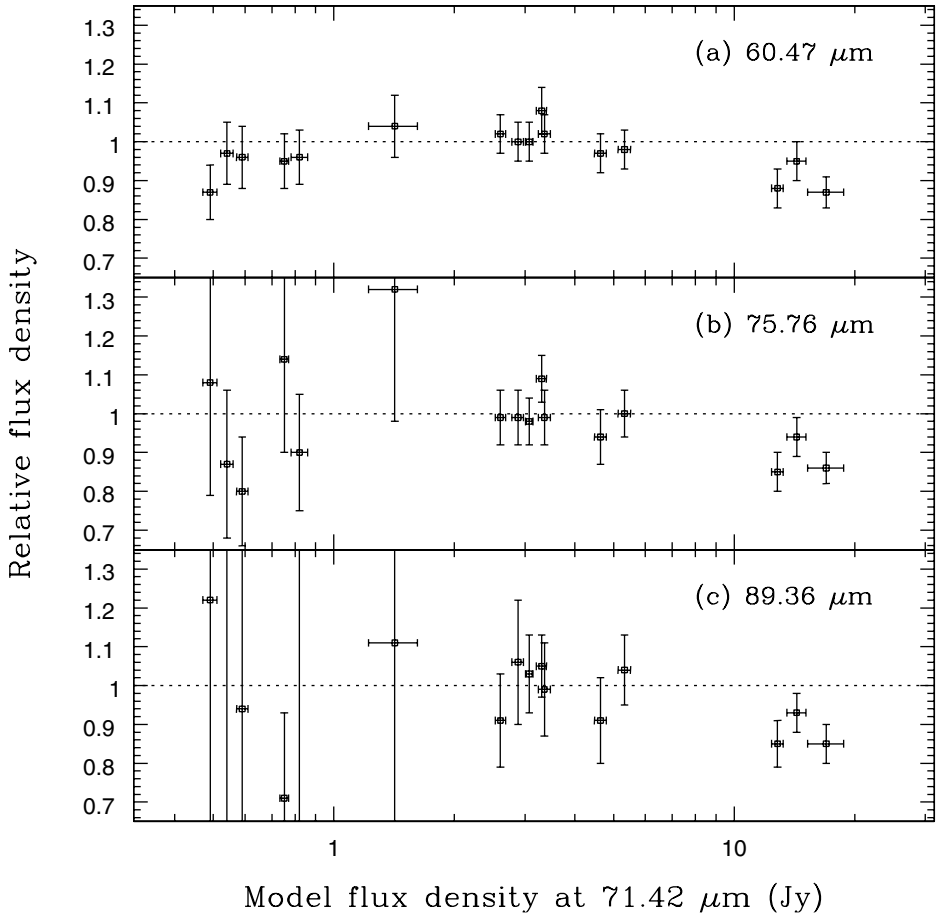

FIG. 8.—Ratio of the predicted MIPS photometric flux densities to the SED-mode flux densities at wavelengths of (*a*) 60.46 μm, (*b*) 75.76 μm, or (*c*) 89.36 μm, as a function of the 71.42 μm model flux density.

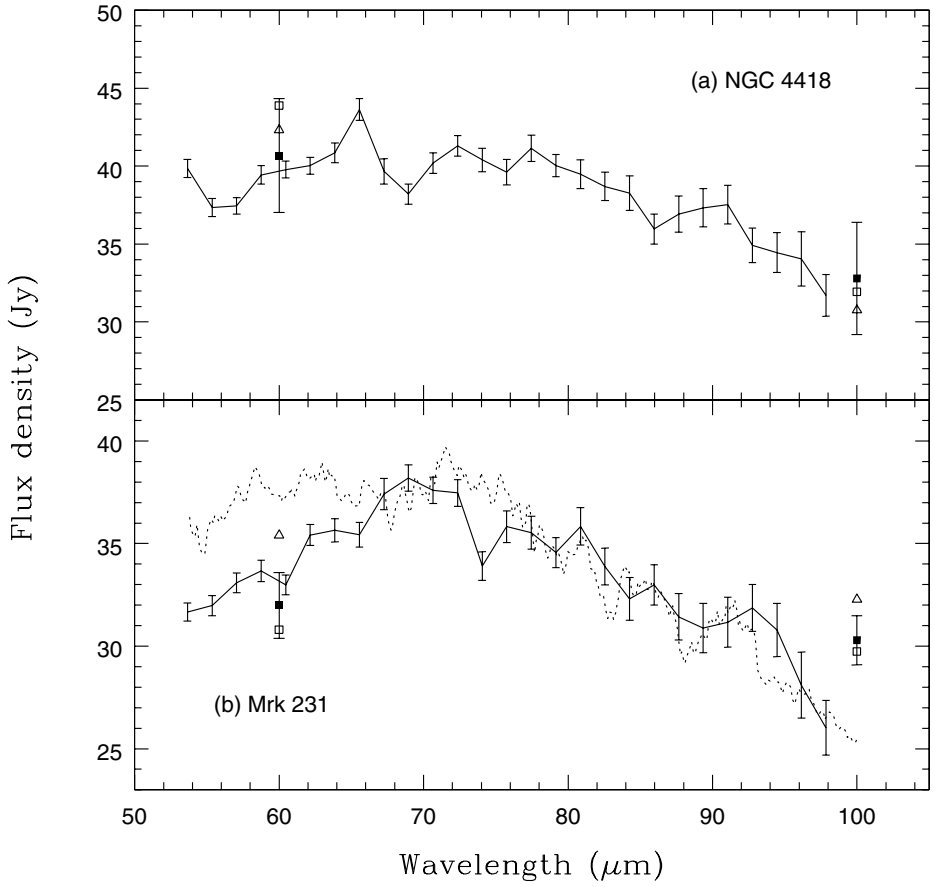

FIG. 9.—Comparisons of the SED-mode measurements (*solid lines*) with *IRAS* 60 and 100 μm observations (*squares and triangles*) for the galaxies NGC 4418 (*a*) and Mrk 231 (*b*). For the latter, an *ISO* LWS spectrum (*dotted line*), obtained from the *ISO* archive (observation identifier 18001306) and smoothed using a 7-pixel boxcar, is also shown. Multiple sources for the *IRAS* data are shown: *IRAS* Faint Source Catalog (*solid squares*), Sanders et al. (2003; *open squares*) and Soifer et al. (1989; *open triangles*). The *IRAS* flux uncertainties are plotted only for the solid squares.

position angle of 119°. A raster step size equal to the width of the SED slit was used so that the map covers the entire optical extent of the system with no spatial gaps. Figure 10 compares an *ISO* LWS spectrum of Arp299 with the spatially integrated MIPS spectrum within a rectangular aperture of $78.4'' \times 88.2''$. This aperture size is slightly larger than the circular LWS beam, whose diameter ranges from 84.6″ to 77.2″ over 50–100 μm (Gry et al. 2003). The overall agreement between the *ISO* and *Spitzer* spectra is better than 15%.

7. SUMMARY

We have described in this paper the calibration of the SED mode of MIPS, based on the current calibration status of the instrument (as of *Spitzer* Pipeline version S17). Our main points are: (1) The SED optical system is stable, has a dispersion of 1.7 μm per detector pixel, and covers 52.8–98.7 μm over detector rows 1–27. (2) The final five detector rows are contaminated by the second-order diffracted light, and are not calibrated. (3) The first detector column should be excluded in any subsequent analysis of SED-mode data. (4) The illumination correction has a column residual variation on the order of 5%. (5) The observed PSF shows some excessive light and asymmetry at radii $>50''$ when compared with the prediction from *Spitzer* Tiny Tim model. This adds an additional uncertainty of up to 10% in the flux calibration of extended sources.

TABLE 5
ERROR BUDGET FOR FLUX CALIBRATION OF EXTENDED SOURCES

Error Source	Estimated Error
Point-source flux uncertainty	$\leq 10\%$
Residual IC uncertainty:	$\sim 5\%$
Aperture-correction uncertainty	$<10\%$
Total[a]:	$<15\%$

[a]The total error squared equals the quadratic sum of the three individual errors.

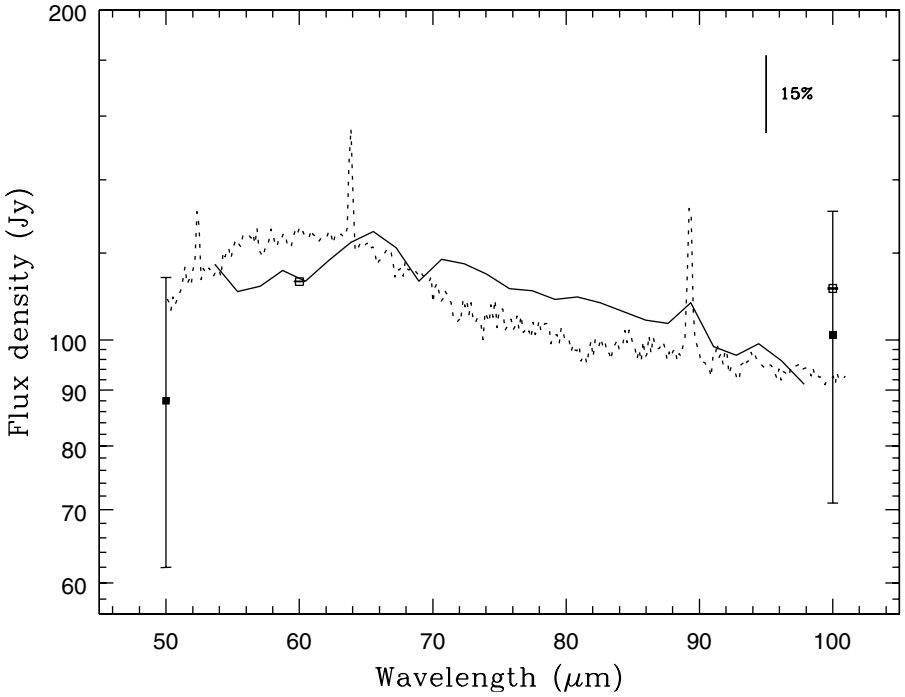

FIG. 10.—Comparison of the spatially integrated SED-mode spectrum (*solid line*) with the *ISO* LWS spectrum (*dotted line*) for the extended galaxy system Arp 299. The LWS spectrum is derived from an *ISO* archival observation (identifier 18001306). Also shown are measurements from *IRAS* (Sanders et al. 2003; *open squares*) and Kuiper Airborne Observatory (Joy et al. 1989; *solid squares*).

(6) Point-source flux calibration is accurate to 10% or better, down to ~0.5 Jy at the blue end of the spectrum, and to ~2 Jy near the red end. (7) No significant flux nonlinearity is seen over a 70 μm flux density range of 0.5–40 Jy. (8) The corresponding surface brightness accuracy for extended sources is estimated to be $\lesssim$15%, due to additional uncertainties in the illumination and aperture corrections.

This work is based on observations made with the *Spitzer Space Telescope*, which is operated by the Jet Propulsion Laboratory, California Institute of Technology under NASA contract 1407. This work was also supported by the MIPS IT contract 1255094 to the University of Arizona. P. S. S. acknowledges support from JPL contract 1256424 to the University of Arizona.

REFERENCES

Engelbracht, C. W., et al. 2007, PASP, 119, 994
Gordon, K. D., et al. 2005, PASP, 117, 503 (GRE05)
Gordon, K. D., et al. 2007, PASP, 119, 1019 (GEF07)
Gry, C., et al. 2003, The ISO Handbook, Vol. III, LWS—The Long Wavelength Spectrometer (Noordwijk: ESA)
Houck, J. R., et al. 2004, ApJS, 154, 18
Joy, M., Lester, D. F., Harvey, P. M., Telesco, C. M., Decher, R., Rickard, L. J., & Bushouse, H. 1989, ApJ, 339, 100
Kennicutt, R. C., Jr., et al. 2003, PASP, 115, 928
Krist, J. 2002, Tiny Tim/SIRTF User's Guide, Tech. Rep. (Pasadena: SSC)
Low, F. J., Smith, P. S., Werner, M. W., Christine, C., Krause, V., Jura, M., & Hines, D. C. 2005, ApJ, 631, 1170
Rieke, G. H., et al. 2004, ApJS, 154, 25
Sanders, D. B., Mazzarella, J. M., Kim, D. C., Surace, J. A., & Soifer, B. T. 2003, AJ, 126, 1607
Soifer, B. T., Boehmer, L., Neugebauer, G., & Sanders, D. B. 1989, AJ, 98, 766
Werner, M. W., et al. 2004, ApJS, 154, 1